We are IntechOpen,
the world's leading publisher of
Open Access books
Built by scientists, for scientists

4,800
Open access books available

122,000
International authors and editors

135M
Downloads

Our authors are among the

154
Countries delivered to

TOP 1%
most cited scientists

12.2%
Contributors from top 500 universities

CLARIVATE ANALYTICS

BOOK CITATION INDEX

INDEXED

WEB OF SCIENCE™

Selection of our books indexed in the Book Citation Index
in Web of Science™ Core Collection (BKCI)

Interested in publishing with us?
Contact book.department@intechopen.com

Numbers displayed above are based on latest data collected.
For more information visit www.intechopen.com

Graphene-Enhanced Optical Signal Processing

Jian Wang and Xiao Hu

Additional information is available at the end of the chapter

Abstract

Graphene has emerged as an attractive material for a myriad of optoelectronic applications due to its variety of remarkable optical, electronic, thermal and mechanical properties. So far, the main focus has been on graphene based photonics and optoelectronics devices. Due to the linear band structure allowing interband optical transitions at all photon energies, graphene has remarkably large third-order optical susceptibility $\chi^{(3)}$, which is only weakly dependent on the wavelength in the near-infrared frequency range. Graphene possesses the properties of the enhancement four-wave mixing (FWM) of conversion efficiency. So, we believe that the potential applications of graphene also lies in nonlinear optical signal processing, where the combination of its unique large $\chi^{(3)}$ nonlinearities and dispersionless over the wavelength can be fully exploited. In this chapter, we give a brief overview of our recent progress in graphene-assisted nonlinear optical device which is graphene-coated optical fiber and graphene-silicon microring resonator and their applications, including degenerate FWM based tunable wavelength conversion of quadrature phase-shift keying (QPSK) signal, two-input optical computing, three-input high-base optical computing, graphene-silicon microring resonator enhanced nonlinear optical device for on-chip optical signal processing, and nonlinearity enhanced graphene-silicon microring for selective conversion of flexible grid multi-channel multi-level signal.

Keywords: graphene, optical nonlinearities, four-wave mixing (FWM), wavelength conversion, quadrature phase-shift keying (QPSK), optical computing, silicon microring resonators, graphene-silicon microring resonator (GSMR), all optical signal processing, on-chip all optical signal processing

1. Introduction

Graphene, a monolayer of carbon atoms arranged in a two-dimensional honeycomb lattice, is a basic building block for graphitic materials of all other dimensionalities. In 2004, a research team based in Manchester successfully isolated graphene by mechanical exfoliation [1]. Since then, many extraordinary properties have been reported, such as extremely high mobility of charge carrier 200,000 $cm^2 V^{-1} s^{-1}$. Graphene possesses linear, massless band structure $E_{\pm}(p) = \pm V|p|$, where the upper (lower) sign corresponds to the electron (hole) band, p is the quasi-momentum, and $V \approx 10^6$ m/s is the Fermi velocity. The high mobility of charge carriers and zero bandgap of graphene can be employed as an ideal medium for high-frequency applications, such as radio-frequency switches [2].

The photonic properties of graphene are equally remarkable. On the one hand, many breakthroughs in research on graphene, including ultrafast photodetectors [3], broadband polarizers [4], and modulators [5], benefit from its unique band structure. The graphene electro-absorption modulator [5] is based on interband transitions, which can be tuned by applying drive voltage, correspondingly changing the Fermi energy (E_F) of graphene. Here, it has to emphasize that at the short wavelength range (that is, infrared and visible), the graphene optical absorptions are determined by interband transitions, whereas at the long wavelength range (that is, terahertz), they are dominated by intraband transitions. In the mid- to far-infrared and THz ranges, graphene exhibits a strong plasmonic response. Doped and patterned graphene can support localized plasmonic resonances, which significantly enhance the absorption [6]. On the other hand, the interband optical absorption in zero-gap graphene could be saturated readily from the visible region to the near-infrared region under strong excitation due to Pauli blocking [7]. Graphene could behave as a fast saturable absorber over a wide spectral range for the mode locking of fiber lasers. Since 2009, a wide variety of laser configurations and operational wavelengths [7–11] is based on graphene mode-locked lasers. Graphene has been suggested as a material that might have large $\chi^{(3)}$ nonlinearities, which is also due to its linear band structure allowing interband optical transitions at all photon energies. It has been indicated [12] that the nonlinear response of graphene is essentially dispersionless over the wavelength and much stronger compared to bulk semiconductors. It has been experimentally demonstrated that the nonlinear refractive index of graphene is as $n_2 \approx 10^{-7}$ $cm^2 W^{-1}$ [13] using the Z-scan technique. After that, optical bistability, self-induced regenerative oscillations, and four-wave mixing (FWM) have been consecutively observed in graphene-silicon hybrid optoelectronic devices [14]. FWM has also been demonstrated in graphene in various configurations, e.g., slow-light graphene-silicon photonic crystal waveguide [15], graphene optically deposited onto fiber ferrules [16], and graphene-coated microfiber [17, 18]. Moreover, FWM-based wavelength conversion of a 10-Gb/s non-return-to-zero (NRZ) signal with mechanically exfoliated graphene was first reported in Ref. [19]. Advanced optical modulation formats play an important role in enabling high-capacity optical transport networks [20] where wavelength conversion function is highly desired.

All-optical wavelength conversions have been studied by many previous works using semiconductor optical amplifiers (SOAs), highly nonlinear fibers (HNLFs), and periodically poled lithium niobates (PPLNs). Silicon-on-insulator (SOI) waveguides feature low cost,

ultra-compact footprint and are compatible with standard metal-oxide-semiconductor (CMOS) technology, comparing to SOAs, HNLFs, and PPLNS. The nonlinear interaction will also be strongly enhanced in silicon waveguide due to its tight light confinement. To further enhance the nonlinear interaction in silicon waveguide devices, resonator structures such as microrings, microdisks, and photonic crystal nanocavities can be introduced. Among these integrated resonant structures, microring resonator has been attractive to researcher in the past several years mainly because of its small size and potential for telecom and datacom applications. Microring resonators have accelerated the demonstration of very low power continuous-wave (CW) nonlinear optics, and similar benefits are expected for its operation in processing high bandwidth optical signal. For applications to optical data signal processing, the main challenge is that the bandwidth of the microring must be large enough to contain all the spectral components of the optical signals. Additionally, all-optical wavelength conversions of advanced optical modulation formats have not been realized in integrated microring structures.

In this chapter, we go over our recent progress in graphene-assisted nonlinear optical device and their applications, including degenerate FWM-based tunable wavelength conversion of QPSK signal [21], two-input optical high-base hybrid doubling and subtraction functions [22], three-input high-base optical computing [23], graphene-silicon microring resonator-enhanced nonlinear optical device for on-chip optical signal processing [24], and nonlinearity enhanced graphene-silicon microring for selective conversion of flexible grid multi-channel multi-level signal.

2. Optical properties of graphene

The primary mechanism of optical absorption in graphene involves two processes: carrier intraband transitions and interband transitions [25–27]. For short wavelengths (that is, infrared and visible range), the graphene optical absorption is determined by interband transitions, whereas for long wavelengths (that is, terahertz range), it is dominated by intraband transitions. **Figure 1** pictorially depicts the basic mechanisms. Interband transitions refer to an exchange of charge carriers between the conduction and valence bands, the energy of a photon $\hbar\omega$ should be satisfying the relationship $\hbar\omega \geq 2E_F$ as shown in **Figure 1(a)**. For n-doped graphene, the optical photon ($\hbar\omega_2$) with energy less than $2E_F$ cannot be absorbed which is because of the electron states in resonance occupied the conduction band. For p-doped graphene, the optical photon ($\hbar\omega_2$) with energy less than $2E_F$ cannot be absorbed which is due to the unavailable electrons for the interband transition. For the low frequency THz range ($\hbar\omega \leq 2E_F$), the intraband absorption mechanism is shown in **Figure 1(b)**. And graphene behaves like a conductive film and its optical conductivity closely follows its electrical conductivity, which can be described by a simple Drude model.

Due to the linear band structure of graphene allowing interband optical transitions at all photon energies, graphene is considered to be a material that might have large $\chi^{(3)}$ nonlinearities. In Ref. [12], the principle of graphene-based degenerate FWM is proposed. Two continuous-wave (CW) pumps with frequencies ω_1 and ω_2 are combined together graphene-based device with high third-order nonlinearity ($\chi^{(3)}$) and mix together to generate a new coherent beam with frequency ω_{con} (converted idler), as depicted in **Figure 2**.
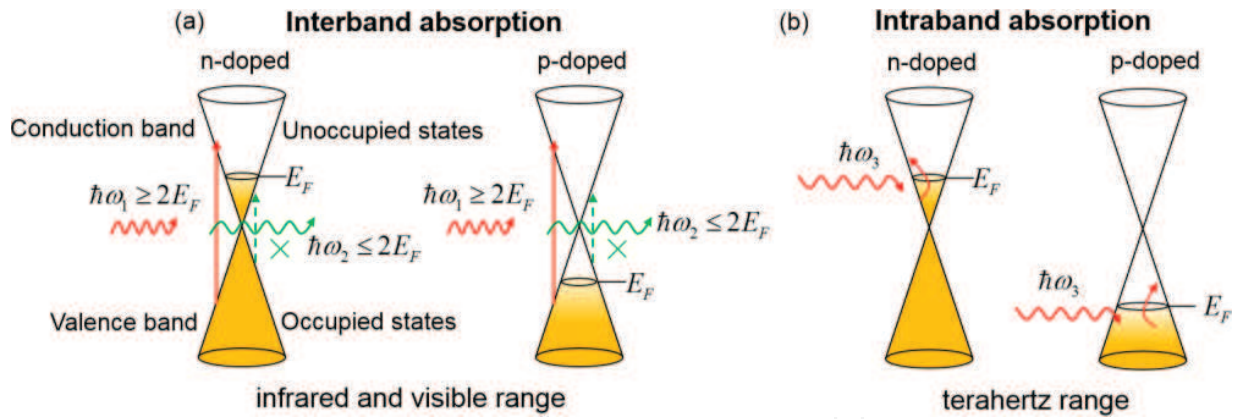
Figure 1. (a) Interband and (b) intraband absorption mechanisms in graphene.
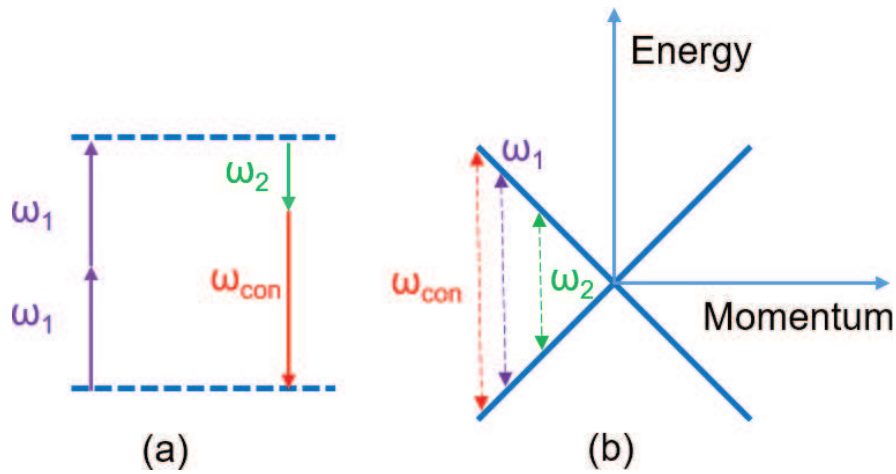

Figure 2. (a) Diagram of energy conservation in the degenerate FWM process. (b) Band structure of graphene with the three resonant photon energies (arrows) involved in degenerate FWM.

3. Fabrication and characterization of graphene-assisted nonlinear optical devices

There is a wide choice in terms of size, quality, and price for any particular graphene-based application: (1) for the liquid phase and thermal exfoliation method, the produced graphene or reduced graphene oxide flakes are suited for composite materials, conductive paints, and so on; (2) for the method of synthesis on SiC, the ultrahigh quality graphene with crystallites approaching hundreds of micrometers in size can be used for high-performance electronic devices; and (3) for chemical vapor deposition (CVD) method, the fabricated large-area uniform polycrystalline graphene films are ready for use in lower-performance active and nonactive devices. Here, considering the quality, size, and price of graphene, we choose the CVD method to grow graphene. Then, the prepared graphene was connected with single mode fiber and silicon microring resonator.

3.1. Graphene-coated optical fiber device

Monolayer graphene was grown by the chemical vapor deposition (CVD) method [28]. Graphene was primarily grown on Cu foils (25-µm thick with a purity of >99.99 wt% obtained from Alfa Aesar) in a hot wall furnace. The growth process can be briefly summarized as follows: (1) load the fused silica tube with the Cu foil, evacuate, back fill with hydrogen, heat to 1050°C and maintain a $H_2(g)$ pressure of 42 mTorr under a 2.5 sccm flow; (2) stabilize the Cu film at the desired temperature, up to 1050°C, and introduce 40 sccm of $CH_4(g)$ for a desired period of time at a total pressure of 450 mTorr; (3) after exposure to CH_4, cool the furnace to room temperature. Then, poly(methyl methacrylate) (PMMA) film was spin coated on the surface of the graphene-deposited Cu foil. Then the Cu foil was etched away with 1 M $FeCl_3$ solution. The resultant PMMA/graphene film (5 mm × 5 mm) was washed in deionized water several times and transferred to the Si/SiO_2 substrate or deionized water solution for next step. To fabricate the graphene-coated optical fiber device, the floating PMMA/graphene sheet was mechanically transferred onto the fiber pigtail cross-section and dried in a cabinet. After drying at room temperature for about 24 hours, the carbon atoms could be self-assembled onto the fiber end-facet, thanks to the strong viscosity of graphene. The PMMA layer can be removed by boiling acetone. By connecting this graphene-on-fiber component with another clean and dry FC/PC fiber connector, as shown in **Figure 3**, the nonlinear optical device was finally constructed and used to FWM-based wavelength conversion applications.

3.2. Graphene-silicon microring resonator (GSMR)

The fabrication process of the nonlinearity enhanced GSMR is shown in **Figure 4**. We fabricate the nonlinearity enhanced GSMR on a commercial SOI wafer with a 340-nm-thick silicon slab
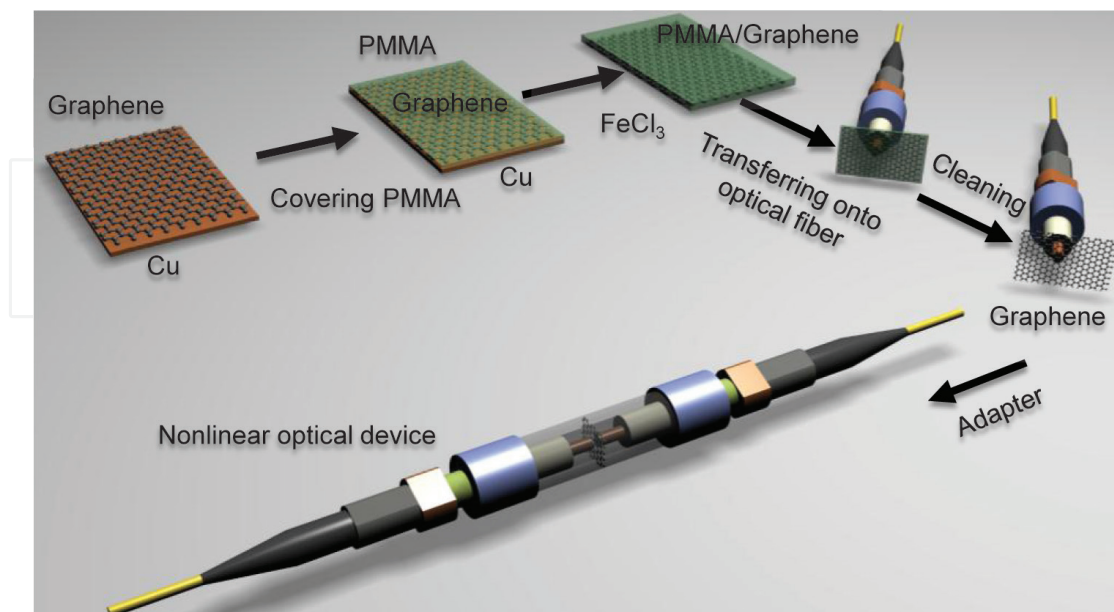

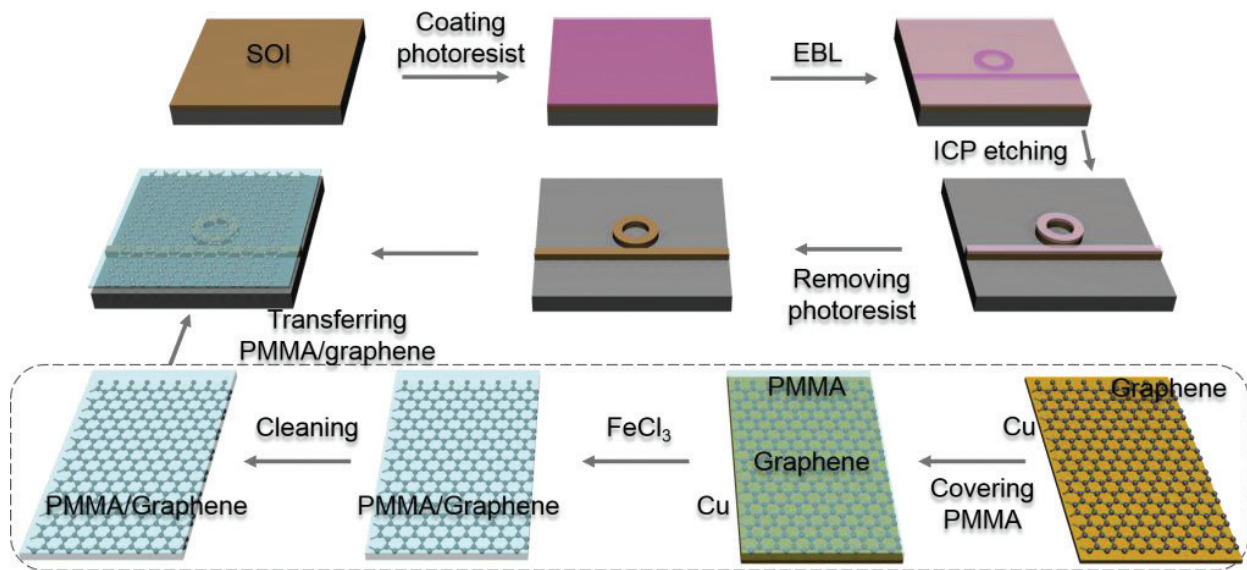**Figure 3.** Fabrication process of the graphene-assisted nonlinear optical device.

Figure 4. Fabrication process of the GSMR.

on the top of a 3-µm silica buffer layer. First, the device pattern is transferred to photoresist by E-beam lithography (EBL). The upper silicon layer is etched downward for 200 nm to form a ridge waveguide through induced coupled plasma (ICP) etching. After removing the photoresist, a silicon microring resonator was fabricated. Second, monolayer graphene was grown on a Cu foil (25-µm thick with a purity of >99.99 wt% obtained from Alfa Aesar) by the chemical vapor deposition method [28]. Poly(methyl methacrylate) (PMMA) film was next spin coated on the surface of the graphene-deposited Cu foil, and the Cu foil was etched away with 1 M FeCl$_3$ solution. The resultant PMMA/graphene film was then washed with deionized water several times. Finally, the floating PMMA/graphene sheet was mechanically transferred onto the top of silicon microring resonator.

Figure 5(a) illustrates the Raman spectrum of the transferred graphene on the silicon microring resonator. Compared to pristine graphene, the blue shifts of the positions of the G and 2D peaks are consistent to the nature of the p-doped graphene [29]. Additionally, the intensity ratio of the 2D to the G peak is about 1.8, significantly smaller than that of the pristine graphene (4–5), which is another evidence of the p-doped graphene [38]. The heavily p-doped graphene is particularly fabricated to achieve optical transparency in the infrared with negligible linear losses, which can be explained as follows: due to the p-doping of graphene, the Fermi level (E_F) is lower than half the photon energy (−vh/2, blue dashed line) and there are no electrons available for the interband transition [5] (**Figure 5(b)**) and intraband graphene absorption is near-absent in the infrared [30]. The device consists of a silicon microring resonator coupled to a straight waveguide with a gap of 150 nm. The waveguide is bidirectional tapered up to a width of 20 µm over a length of 600 µm to connect dual TE-polarized grating couplers. A scanning electron micrograph (SEM) of the fabricated GSMR resonator with partial part of the straight waveguide is shown in **Figure 5(c)**. It is fabricated by standard complementary metal-oxide-semiconductor (CMOS) processes on an SOI substrate with a 3 µm-thick buried oxide layer. The width and height of the ridge waveguide in
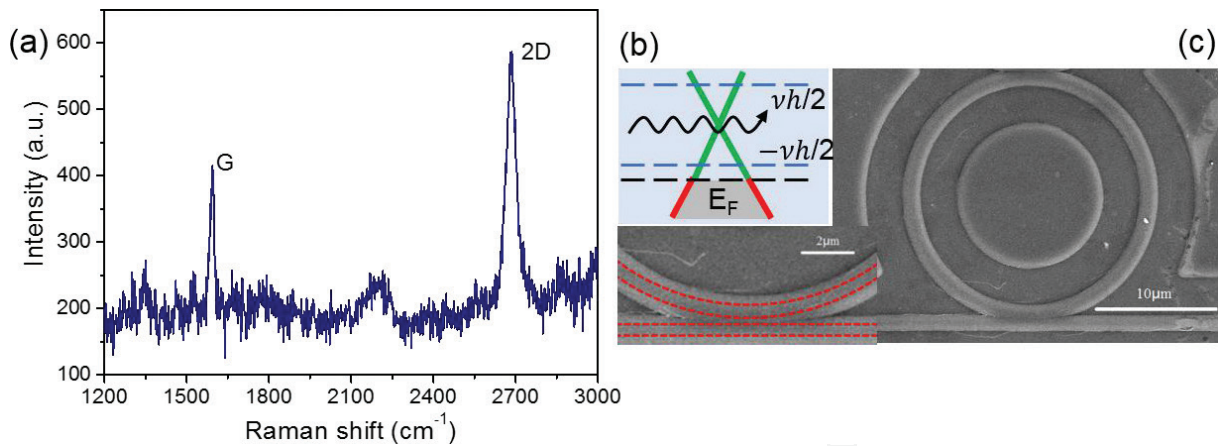
Figure 5. (a) Raman spectrum of the single-layer graphene sample. (b) The doped principle: the Fermi level (E_F) less than half the photon energy ($-vh/2$, blue dashed line), therefore, there are no electrons available for the interband transition. (c) SEM image of the GSGM resonator. The inset shows the detailed view of the coupling region. Red-dashed lines show the outline of the silicon waveguides.

the structure are 450 and 200 nm, respectively. The total insertion loss is about 10 dB at input wavelength of 1550 nm. Here, the input power is defined as the power in the straight wave-guide coupled into the silicon microring resonator. We use standard polymer-based transfer method to cover a graphene sample on the top of the silicon waveguide and the detailed picture of the straight waveguide coupled with an arc region of the microring resonator is shown in the inset of **Figure 5(c)**. Due to the deposition of polymer on the GSMR, the gap is covered and the silicon waveguides before transfer are marked with red-dashed lines.

4. Graphene-enhanced nonlinear optical device for optical transport networks signal processing

It is well known that advanced optical modulation formats have become of great impor-tance to enable high-capacity optical transport networks [20] where wavelength conversion function is highly desired. The nonlinear response of graphene is very high and essentially dispersionless over the wavelength. Such nonlinearity of graphene can be utilized to realize various nonlinear functional devices for telecommunication networks, such as, wavelength converters.

4.1. Degenerate FWM-based tunable wavelength conversion of QPSK signal

Figure 6 shows the experimental set-up for degenerate FWM-based wavelength conversion using a single-layer graphene grown by the CVD method [21]. The CW output from an exter-nal cavity laser (ECL1) serves as the signal light for the degenerate FWM and is modulated with QPSK signal at 10 Gbaud by a single-polarization optical I/Q modulator. An arbitrary waveform generator (AWG) running at a 10 GS/s sampling rate is used to produce the elec-trical signal. The modulated 10 Gbaud QPSK signal is then amplified by an erbium-doped
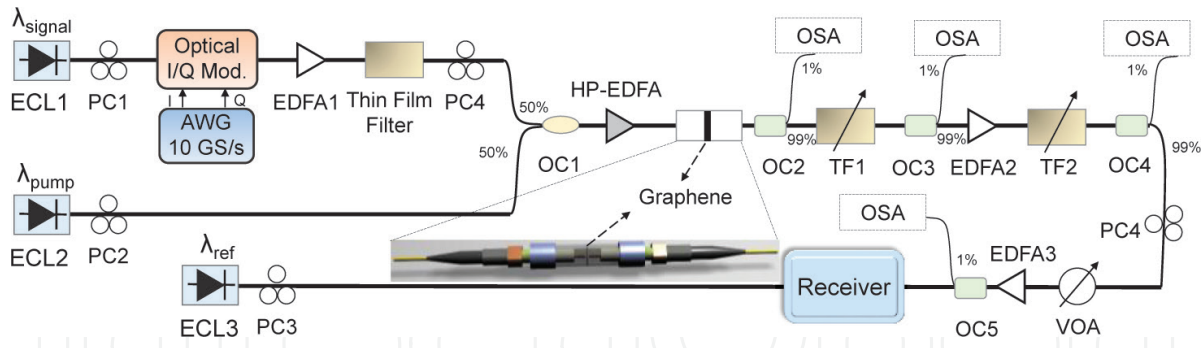
Figure 6. Experimental set-up for degenerate FWM-based wavelength conversion in graphene. Inset: "sandwiched structure" graphene sample used as a nonlinear optical device. ECL: external cavity laser; AWG: arbitrary waveform generator; TF: tunable filter; OC: optical coupler; PC: polarization controller; OSA: optical spectrum analyzer; and VOA, variable optical attenuator.

optical fiber amplifier (EDFA) followed by a thin film filter to suppress the amplified spontaneous emission (ASE) noise. Afterwards, the 10 Gbaud QPSK signal is combined with another CW light from ECL2, which serves as the pump light through a 3-dB coupler, amplified using a high-power EDFA (HP-EDFA), and launched into the single-layer graphene sample. The polarization states of the CW pump and QPSK signal are adjusted to achieve optimized conversion efficiency of degenerate FWM in graphene. The amplified CW pump and QPSK signal take part in the degenerate FWM process when passing through the single-layer graphene sample and a newly converted idler is generated. After the FWM wavelength conversion, the converted idler is selected using two tunable filters (TF1, TF2) for coherent detection. First, the converted idler is selected using TF1. Since the power level of the converted idler is relatively low, the selected converted idler is amplified by EDFA2. Second, in order to suppress the amplified spontaneous emission (ASE) noise originated from EDFA2, another TF2 is employed. Hence, the TF1 is used to select the converted idler, and TF2 is used to suppress the ASE noise. The CW output from ECL3 serves as a reference light for coherent detection. A variable optical attenuator (VOA) and a low noise EDFA (EDFA3) are employed to adjust the received signal-to-noise ratio (OSNR) for bit-error rate (BER) measurements.

To characterize the performance of QPSK wavelength conversion, we further measure the BER curve as a function of the received OSNR for back-to-back (B-to-B) signal and converted idler. **Figure 7** plots measured BER performance for tunable QPSK wavelength conversion with the converted idler generated at 1546.88, 1539.92, and 1557.90 nm, respectively. The power of HP-EDFA is estimated to be 31 dBm. The measured conversion efficiencies for converted idlers at 1546.88, 1539.92, and 1557.90 nm are −36.2, −48.2, and −39.8 dB, respectively. As shown in **Figure 7**, the observed OSNR penalty is around 1 dB at a BER of 1×10^{-3} (7% forward error correction (FEC) threshold) for QPSK wavelength conversion with the converted idler at 1546.88 nm. The received OSNR penalties of ~2.2 dB at a BER of 1×10^{-3} are observed for converted idlers at 1539.92 and 1557.90 nm. The increased OSNR penalty is mainly due to the reduced conversion efficiency for converted idlers at 1539.92 and 1557.90 nm. The right insets of **Figure 7** depict corresponding constellations of the B-to-B signals and converted idlers. The OSNR penalty is believed to be originated from the relatively low conversion efficiency (<−35 dB), which can be ascribed to the very limited interaction between the single-layer graphene and the propagating
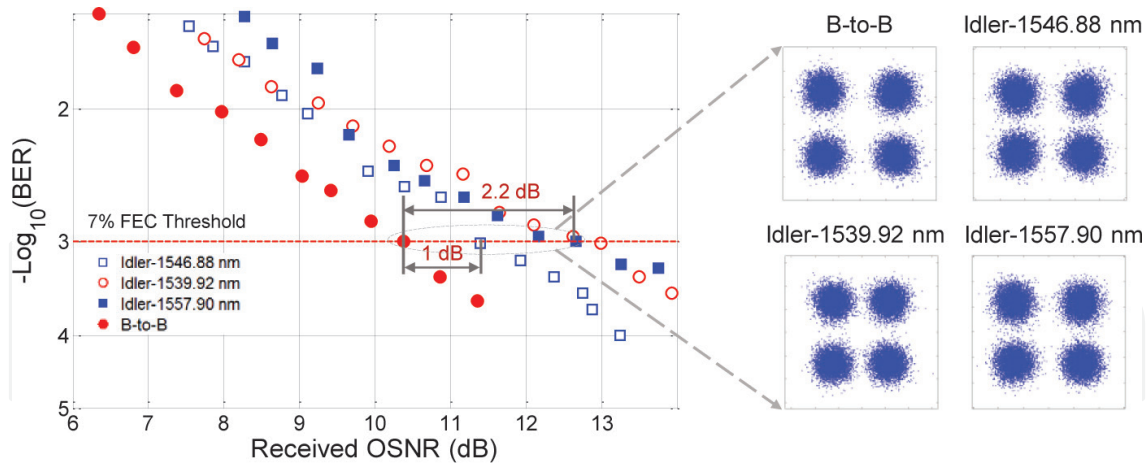
Figure 7. Measured BER versus received OSNR for wavelength conversion of QPSK signal. Insets show constellations of QPSK.

light only at the end face of optical fiber. With further improvement, one might enhance the conversion efficiency by mechanically transferring graphene sample grown by the CVD method onto the D-shaped fiber or microfiber to ensure more direct graphene-light interaction.

4.2. Two-input optical high-base hybrid doubling and subtraction functions

Figure 8 illustrates the concept and principle of two-input hybrid quaternary arithmetic functions [22]. From the constellation in the complex plane (**Figure 8(a)**), it is clear that one can use four-phase levels ($\pi/4$, $3\pi/4$, $5\pi/4$, $7\pi/4$) of (D)QPSK to represent quaternary base numbers (0, 1, 2, 3). To implement two-input hybrid quaternary arithmetic functions, the aforementioned graphene-assisted nonlinear optical device is employed. Two-input quaternary numbers (A, B) are coupled into the nonlinear device, then two converted idlers (idler 1, idler 2) are simultaneously generated by two degenerate FWM processes. **Figure 13(b)** illustrates the degenerate FWM process. We derive the electrical field (E) and optical phase (φ) relationships of two degenerate FWM processes under the pump nondepletion approximation expressed as
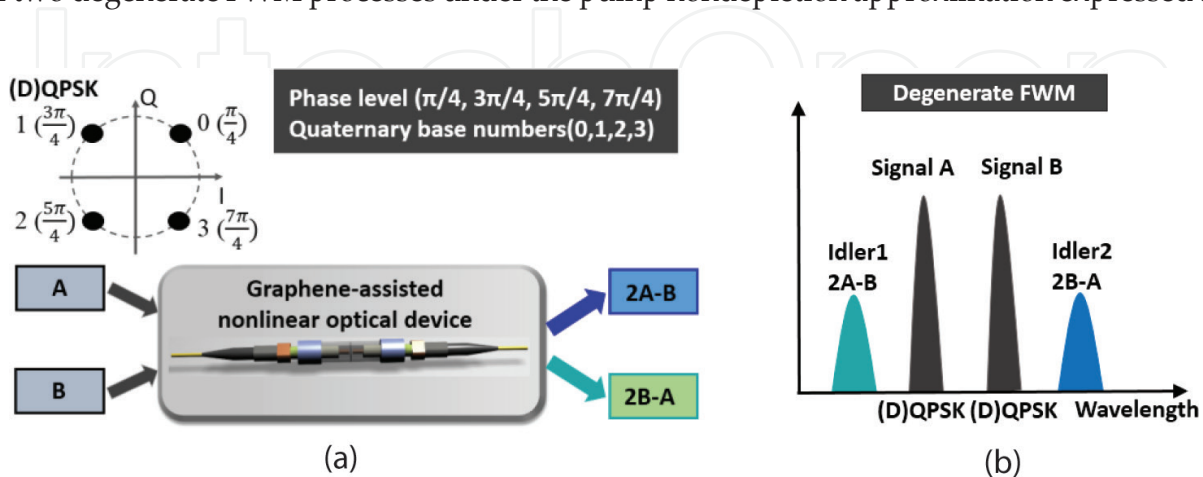

Figure 8. (a) Concept and (b) principle of hybrid quaternary arithmetic functions (2A-B, 2B-A) using degenerate FWM and (D)QPSK signals.

$$E_{i1} \propto E_A \cdot E_A \cdot E_B^*, \quad \varphi_{i1} = \varphi_A + \varphi_A - \varphi_B \tag{1}$$

$$E_{i2} \propto E_B \cdot E_B \cdot E_A^*, \quad \varphi_{i2} = \varphi_B + \varphi_B - \varphi_A \tag{2}$$

where the subscripts A, B, i1, i2 denote input signal A, signal B, converted idler 1, idler 2, respectively. Owing to the phase wrap characteristic with a periodicity of 2π, it is implied from the linear phase relationships in Eqs. (1) and (2) that idler 1 and idler 2 carry out modulo 4 operations of hybrid quaternary arithmetic functions of doubling and subtraction (2A-B, 2B-A).

The measured typical spectrum obtained after the CVD single-layer graphene-coated fiber device is depicted in **Figure 9**. Two 10-Gbaud NRZ-(D)QPSK signals at 1550.10 (A) and 1553.60 nm (B) are employed as two inputs. The power of two input signals (A, B) is set to about 32 dBm. The conversion efficiency is -36 dB. One can clearly see that two converted idlers are obtained by two degenerate FWM processes with idler 1 at 1546.60 nm (2A-B) and idler 2 at 1557.20 nm (2B-A). The resolution of the measured spectrum is set to 0.02 nm. The steps in the measured spectrum are actually the modulation sidebands of two NRZ-(D)QPSK carrying signals. As shown in **Figure 10**, in order to verify the hybrid quaternary arithmetic functions, we measure the phase of symbol sequence for two input signals and two converted idlers. By carefully comparing the quaternary base numbers for two input signals and two converted idlers, one can confirm the successful implementation of two-input hybrid quaternary arithmetic functions of 2A-B and 2B-A.

4.3. Three-input high-base optical computing

We also propose an approach to performing three-input optical addition and subtraction of quaternary base numbers using multiple nondegenerate FWM processes based on graphene-coated fiber device [23]. The concept and principle of three-input high-base optical computing are similar to **Figure 8**. In the experiment, the wavelengths of three-input signals A, B, and C are fixed at 1548.52, 1550.12, and 1552.52 nm, respectively. **Figure 11** depicts the measured typical optical spectrum obtained after the single-layer graphene-coated fiber device. One can clearly see that three converted idlers are generated by three nondegenerate FWM processes
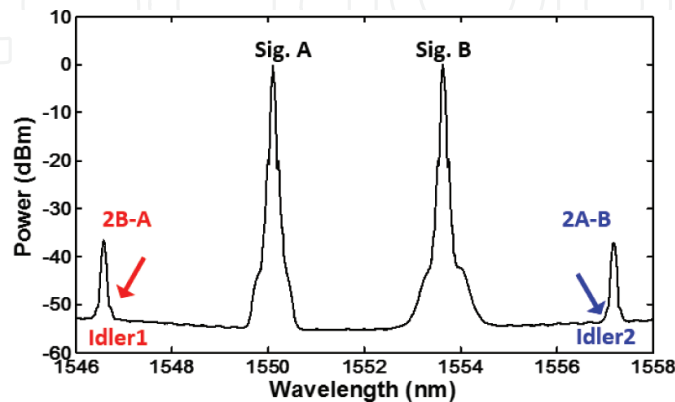

Figure 9. Measured spectrum for 10-Gbaud two-input hybrid quaternary arithmetic functions.
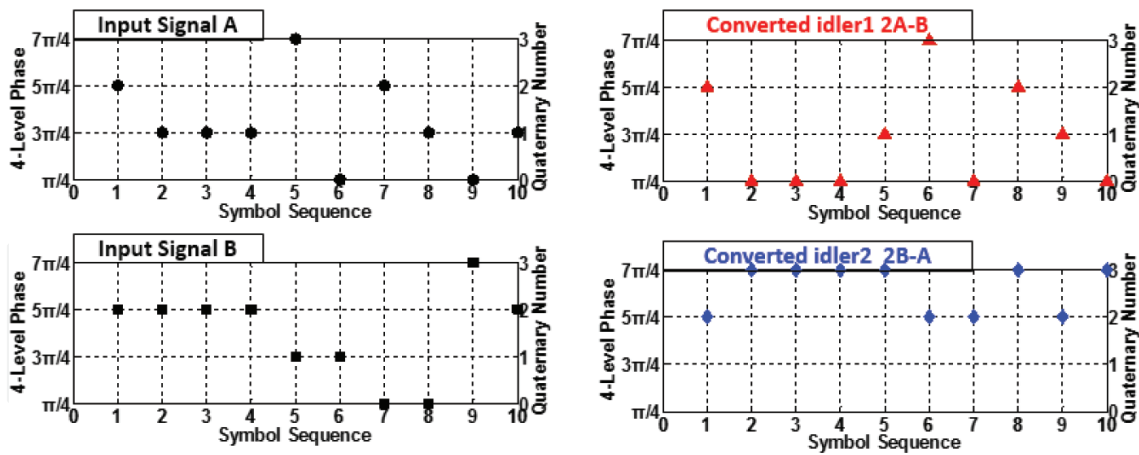
Figure 10. Measured phase of symbol sequence with coherent detection for 10-Gbaud two-input hybrid quaternary arithmetic functions.

with idler 1 at 1546.13 nm (A + B − C), idler 2 at 1550.92 nm (A + C − B), and idler 3 at 1554.13 nm (B + C − A), respectively. The power of HP-EDFA is estimated to be 31 dBm. The conversion efficiencies of three nondegenerate FWM processes are measured to be larger than −34 dB.

To characterize the performance of the proposed graphene-assisted modulo 4 functions of three-input high-base optical computing, we further measure the BER curves as a function of the received OSNR for back to back (B-to-B) signals and three converted idlers. **Figure 12** depicts the measured BER curves for 10-Gbaud modulo 4 operations of three-input quaternary hybrid addition and subtraction of A + B − C, A + C − B, and B + C − A. As shown in **Figure 12**, the observed OSNR penalties for modulo 4 operations of three-input quaternary hybrid addition and subtraction are accessed to be less than 7 dB at a BER of 2×10^{-3} (7% enhanced forward error correction (EFEC) threshold). The increased OSNR penalties might be mainly due to the
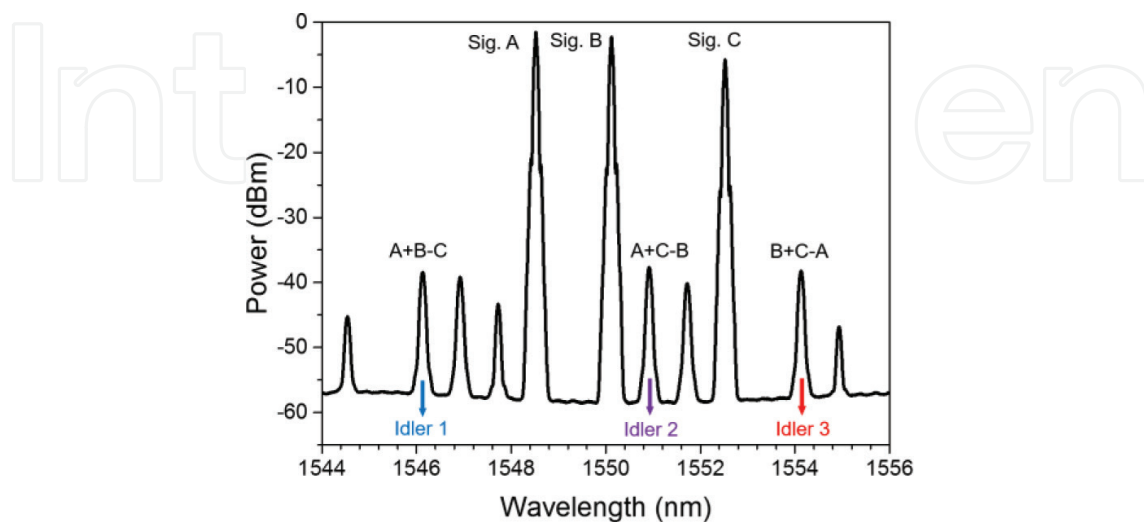

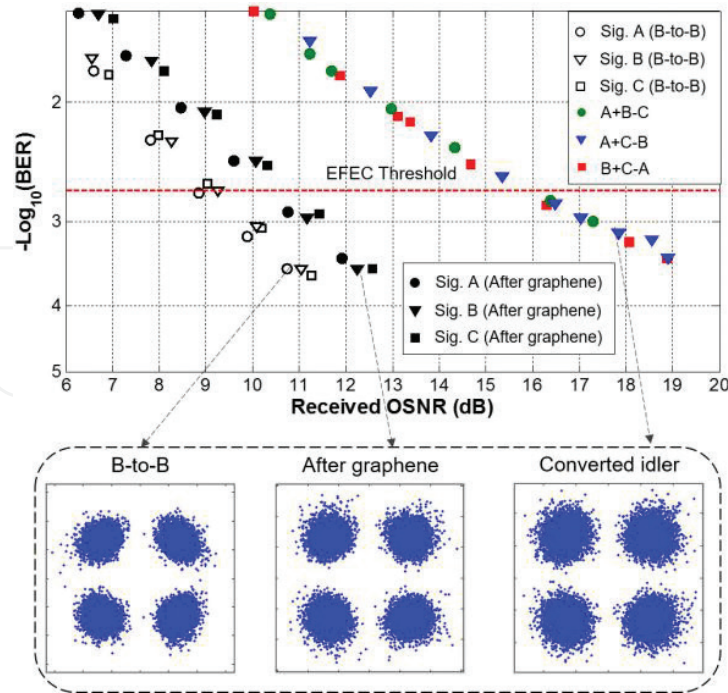**Figure 11.** Measured spectrum for 10-Gbaud three-input quaternary hybrid addition and subtraction.

Figure 12. Measured BER curves for 10-Gbaud modulo 4 operations of three-input quaternary hybrid addition and subtraction of A + B − C, A − C − B, and B + C − A. Insets show constellations of (D)QPSK signals.

relatively low conversion efficiency for converted idlers and accumulated distortions transferred from three-input signals (A, B, and C). The insets in **Figure 12** depict the corresponding constellations of the B-to-B signals and converted idlers. The BER curves and constellations of three output signals (A, B, and C) after graphene are also shown in **Figure 12** for reference.

For the graphene-assisted modulo 4 functions of three-input high-base optical computing, we also study the performance tolerance to the relative time offset between three input signals. **Figure 13** depicts the BER performance as a function of the relative time offset between three signals (signal offset) under an OSNR of ~17 dB. It is found that the BER is kept below EFEC
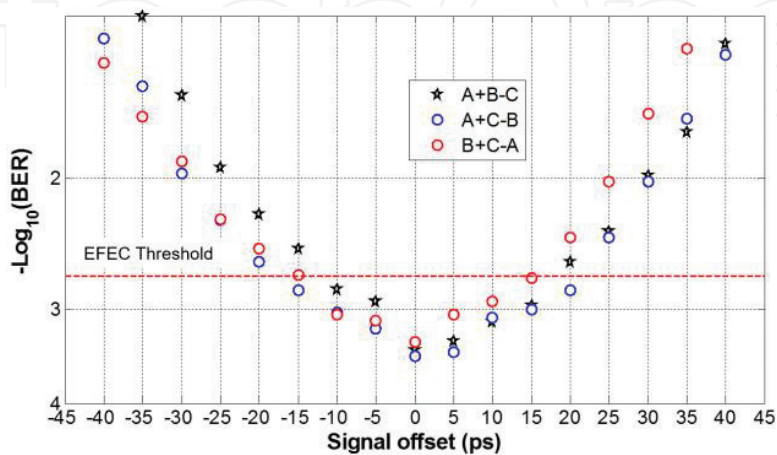

Figure 13. Measured BER performance versus signal offset.

threshold when the signal offset is within 15 ps. The obtained results shown in **Figure 13** indicate a favorable performance tolerance to the signal offset.

5. GSMR-enhanced nonlinear optical device for on-chip optical signal processing

Microring resonators have accelerated the demonstration of very low power continuous-wave (CW) nonlinear optics, and similar benefits are expected for its operation in processing high bandwidth optical signal. Actually, it is only very recently that the first demonstration of optical signal processing based a resonant cavity has been reported. Wavelength conversion at 2.5 Gb/s in a single microring [31] and 10 Gb/s in a silicon-cascaded microring resonator [32] have been demonstrated. On the other hand, it is well known that advanced optical modulation formats have become of great importance to enable high-capacity optically routed transport networks and design of modern wavelength-division multiplexed (WDM) fiber systems [20]. However, all-optical wavelength conversions of advanced optical modulation formats have not been realized in integrated ring structures.

5.1. GSMR-enhanced all-optical up and down wavelength conversion

Figure 14 shows the experimental set-up for degenerate FWM based up and down wavelength conversion using a GSMR [24].

In the experiment, the radius of the silicon microring resonator is 10 μm, and the corresponding free spectral range is around 10 nm. The grating coupler exhibits a 50-nm coupling range with 3-dB coupling loss and the central wavelength of the grating is 1550 nm. Based on the characterization of the fabricated GSMR, two neighboring resonant wavelengths of 1548 and 1558 nm are chosen as the pump and signal light for up wavelength conversion, and the converted idler
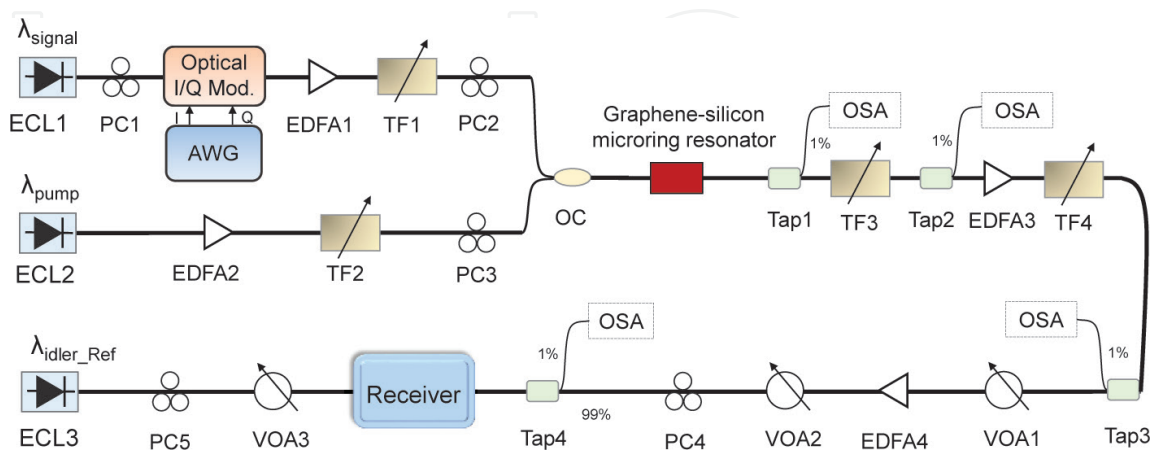

Figure 14. Experimental set-up for degenerate FWM-based up and down wavelength conversion in GSMR. ECL: external cavity laser; AWG: arbitrary waveform generator; EDFA: erbium-doped optical fiber amplifier; TF: tunable filter; OC: optical coupler; PC: polarization controller; OSA: optical spectrum analyzer; and VOA: variable optical attenuator.

wavelength is around 1538 nm. Similarly, for down wavelength conversion, the signal and pump light wavelengths are chosen as 1538 and 1548 nm, and the converted idler wavelength is around 1558 nm. **Figure 15(a)** and **(b)** shows the typical output degenerate FWM spectra obtained after the GSMR for up and down wavelength conversions of QPSK signal.

We define the conversion efficiency as the power ratio of converted idler to signal. **Figure 16(a)** and **(b)** plots the experimentally measured and fitted conversion efficiency as a function of input pump power for up and down wavelength conversion, respectively. The nonlinear Kerr coefficient increment caused by graphene is responsible for the enhanced FWM in the GSMR [33]. One can clearly see that the conversion efficiency increases with the pump power. The saturation of the conversion efficiency at relatively high pump power level results from the two-photon absorption and free carrier absorption in silicon. The device can be tuned by the thermo-optic effect. The resonant wavelength of GSMR as a function of temperature is depicted in **Figure 17**. When the temperature changes from 20 to 40°C, the resonant wavelength can be linearly tuned from 1556.80 to 1559.11 nm. With future improvement, the tuning range of the device can be also remarkably increased by using microheater structures for temperature tuning [34, 35].

To further characterize the performance of QPSK wavelength conversion, we measure the BER curves as a function of the received OSNR for back-to-back signals and up/down converted idler. **Figure 18** plots measured BER performance for QPSK wavelength conversion with the converted idlers generated at 1538.64 nm (up conversion) and 1558.15 nm (down conversion), respectively. The output powers of EDFA1 and EDFA2 are set to be around 25.1 and 25.3 dBm, respectively. The measured conversion efficiencies for converted idlers at 1538.64 nm (up conversion) and 1558.15 nm (down conversion) are −38.34 and −40.2 dB, respectively. The observed OSNR penalties for QPSK up and down wavelength conversion are less than 1.4 dB at a BER of 1×10^{-3} [7% forward error correction (FEC) threshold]. The insets of **Figure 18** depict the corresponding constellations of the back-to-back signals and converted idlers. We also evaluate the BER performance for up wavelength converted idler when the pump power increases from 9.3 to 15.3 dBm. As shown in **Figure 19**, the minimum penalty is less than 0.8 dB when the pump power is 13.3 dBm. The OSNR penalty is around 2 dB with a pump power 9.3 dBm.
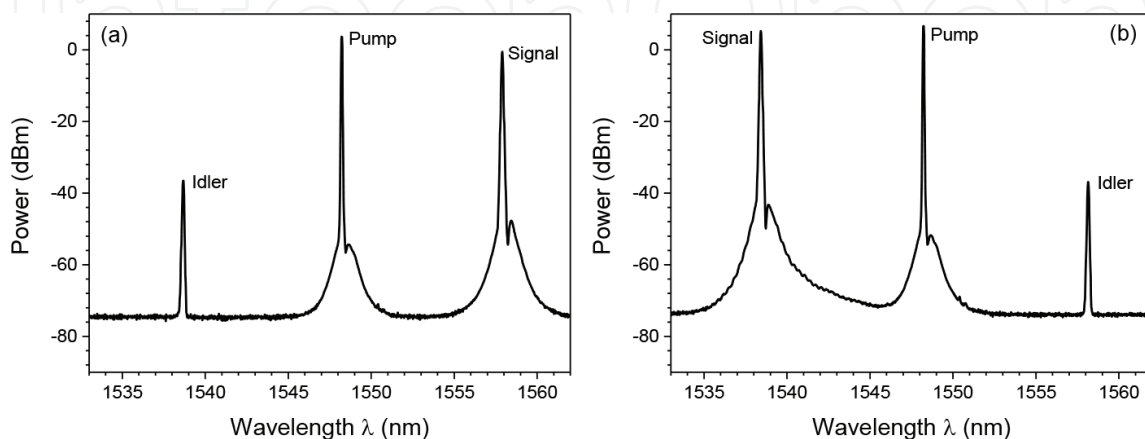

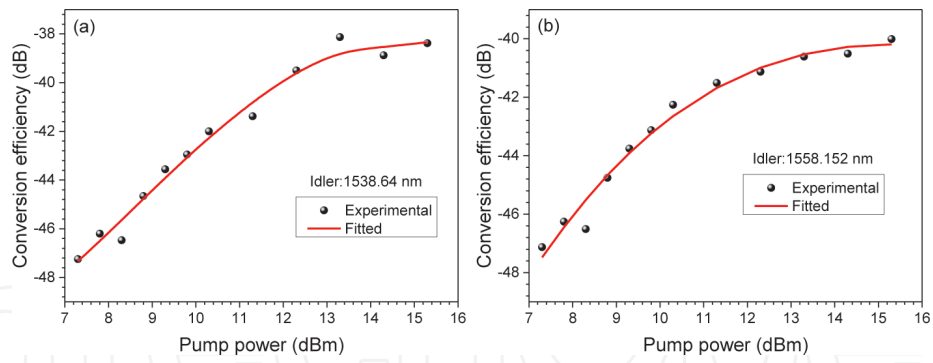**Figure 15.** Measured degenerate FWM spectra for (a) up and (b) down wavelength conversion.

Figure 16. Experimentally measured and fitted conversion efficiency versus input pump power for (a) up and (b) down wavelength conversion.
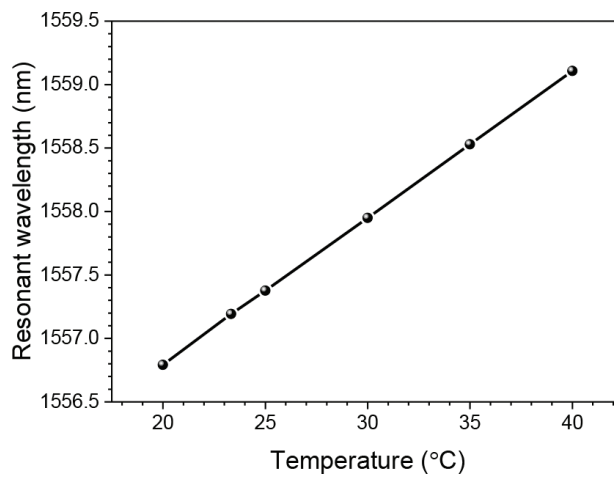

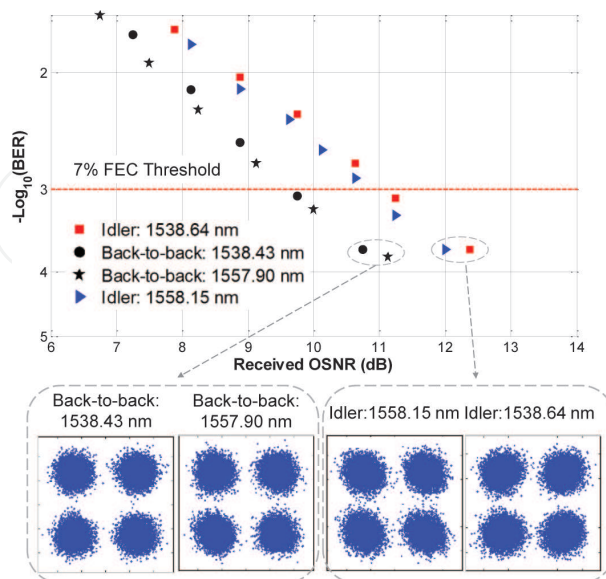**Figure 17.** Measured resonant wavelength of GSMR versus temperature.

Figure 18. Measured BER versus received OSNR for up and down wavelength conversion of QPSK signal. Insets show constellations of QPSK.
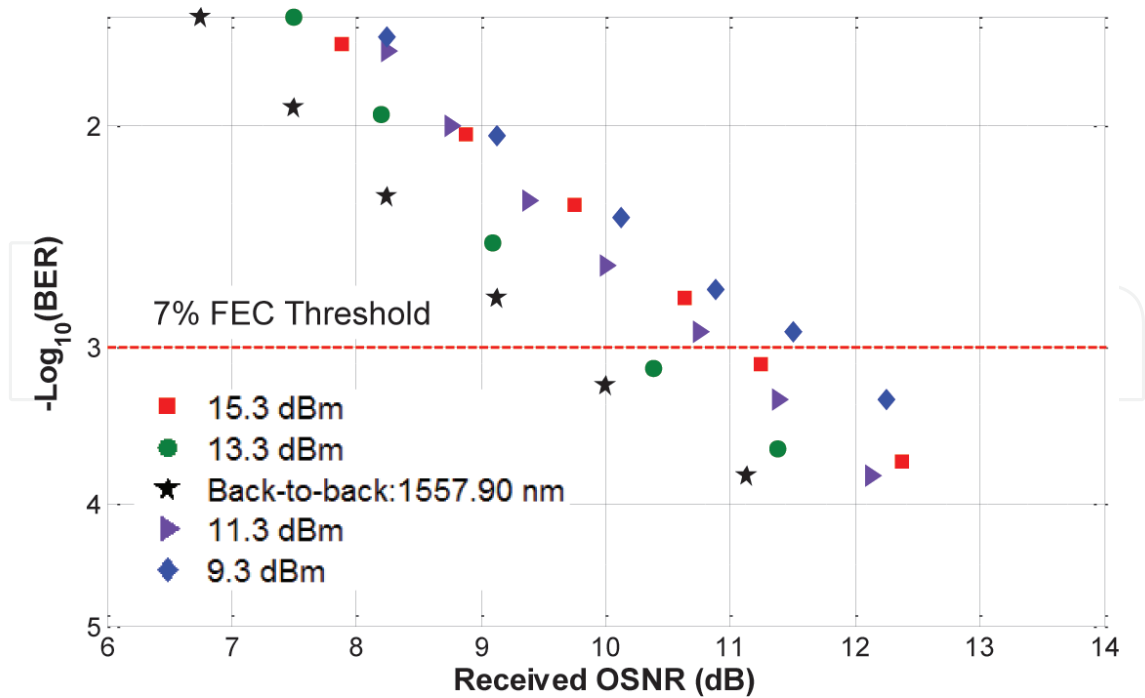
Figure 19. Measured BER versus received OSNR for up wavelength conversion of QPSK signal when pump power increases from 9.3 to 13.3 dBm.

The obtained results shown in **Figures 15–19** imply favorable performance achieved for up and down wavelength conversion of QPSK signal using the fabricated GSMR.

5.2. Nonlinearity enhanced graphene-silicon microring for selective conversion of flexible grid multi-channel multi-level signal

Figure 20 illustrates the concept and operation principle of the GSMR-enhanced FWM for selective conversion of flexible grid multichannel multilevel signal. As shown in **Figure 20(a)**, introducing a resonator structure and graphene to the silicon waveguide can enable enhanced nonlinearity together with channel-selective operation. As shown in **Figure 20(b)**, one continuous-wave (CW) pump and a four-channel flexible grid data-carrying signal are fed into the GSMR. When propagating along the silicon waveguide, pump photons are annihilated to create signal photons and newly converted idler photons by the FWM process. At the output of the silicon waveguide, the data information carried by the input signal is converted to the idlers. Since the resonant dip of the nonlinearity enhanced GSMR is aligned to one of the signals, only the data information of the selected signal light can be converted to the idler. Moreover, the selective conversion operation is transparent to the channel spacing of the multichannel multilevel signal, thus it is compatible with flexible grid optical network. As shown in **Figure 20(c)**, by tuning the pump wavelength and thermal tuning the resonant wavelength of the nonlinearity enhanced GSMR, the desired channel of the flexible grid multichannel multilevel signal can be selected.

We evaluate the system performance of the selective conversion of flexible grid multichannel 16-QAM signal using the nonlinearity enhanced GSMR. **Figure 21(a)–(d)** plot measured the BER performance when the channel spacing is 200, 100, 50, and 20 GHz, respectively. The
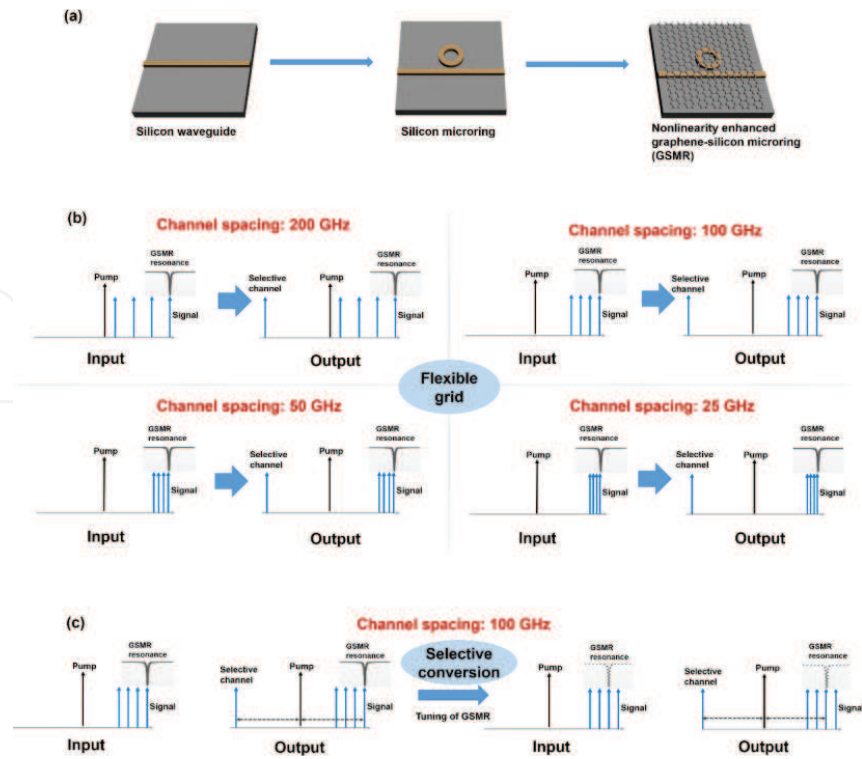
Figure 20. Concept and principle of GSMR-enhanced FWM for channel-selective wavelength conversion of flexible grid multi-channel signal. (a) From silicon waveguide to silicon microring and GSMR with enhanced nonlinearity. (b) Flexible grid. (c) Selective conversion.

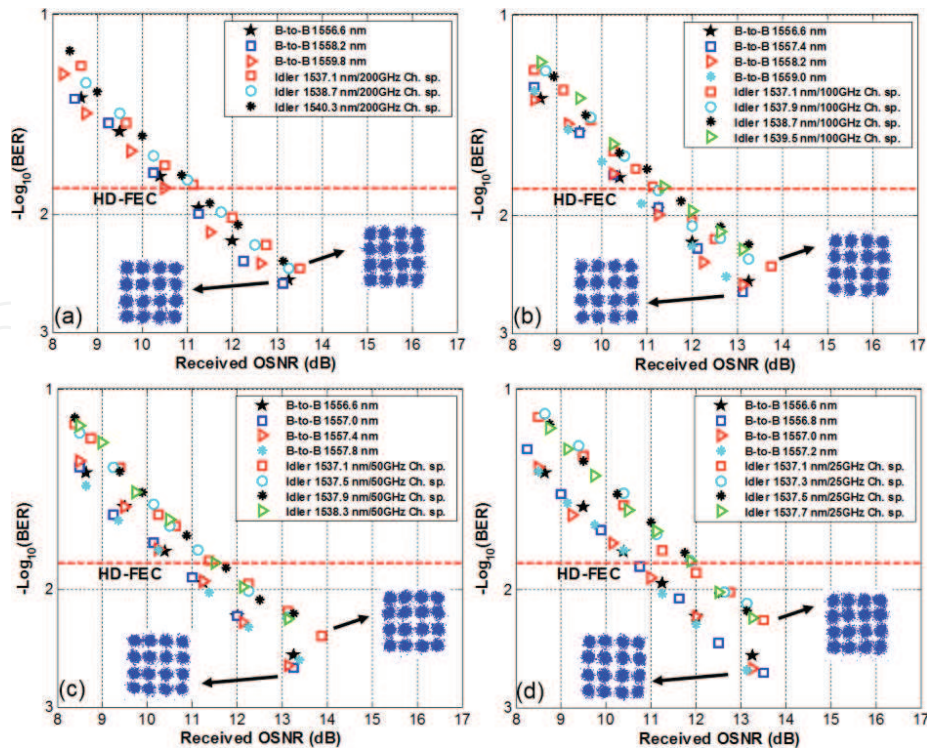

Figure 21. Measured BER curves and constellations of selective conversion of flexible grid multichannel 16-QAM signal in a nonlinearity enhanced GSMR. The channel spacing is (a) 200 GHz, (b) 100 GHz, (c) 50 GHz, and (d) 25 GHz, respectively.

optical signal-to-noise ratio (OSNR) penalties are all below 1 dB for 200, 100, and 50 GHz channel spacing. The OSNR penalties for 25-GHz channel spacing are about 1.2 dB. The insets of **Figure 21(a)–(d)** depict the corresponding constellations of the B-to-B signal and converted idlers. The clear constellations of converted idlers indicate favorable performance achieved for selective conversion of flexible grid multichannel multilevel signal in a nonlinearity enhanced GSMR.

6. Discussions and conclusions

Looking back on the previous works of graphene-assisted nonlinear optical signal processing, Hendry and co-workers experimentally demonstrated the graphene-based FWM for the first time [12]. They also indicated that graphene might have large $\chi^{(3)}$ nonlinearity due to its linear band structure allowing interband optical transitions at all photon energies. After that FWM was also observed in graphene-silicon hybrid optoelectronic devices [14] and graphene-coated microfiber [17, 18]. Moreover, FWM-based wavelength conversion of a 10-Gb/s NRZ signal with mechanically exfoliated graphene was first reported in Ref. [19].

In this chapter, we have reviewed our recent progress in graphene-assisted nonlinear optical device and their applications, including degenerate FWM-based tunable wavelength conversion of quadrature phase-shift keying (QPSK) signal, two-input optical high-base hybrid doubling and subtraction functions, three-input high-base optical computing, graphene-silicon microring resonator enhanced nonlinear optical device for on-chip optical signal processing, and nonlinearity enhanced graphene-silicon microring for selective conversion of flexible grid multichannel multilevel signal.

For FWM-based tunable wavelength conversion of QPSK signal, the total effective nonlinear Kerr coefficient of the graphene-assisted nonlinear optical device is actually the combined contributions from the graphene and the device material (e.g. silica in graphene-coated fiber). It has to emphasize that spectrally efficient advanced modulation formats have been widely used in optical fiber transmission systems. The advanced optical modulation formats play an important role in enabling high-capacity optical transport networks where wavelength conversion function is highly desired. Therefore, exploring wavelength conversion of advanced modulation formats based on FWM in graphene is very interesting and meaningful.

For graphene-assisted optical computing (two-input and three input), the innovative schemes to achieve hybrid quaternary arithmetic functions of doubling and subtraction using optical nonlinearities in graphene and (D)QPSK signals are presented. We experimentally demonstrate 10-Gbaud quaternary arithmetic functions of 2A-B and 2B-A by exploiting degenerate FWM in graphene. The power penalties of converted idlers at a BER of 2×10^{-3} are measured to be about 7.4 dB for 2A-B and 7.0 dB for 2B-A. With future improvement, graphene-assisted nonlinear optical devices might be employed to facilitate more optical signal processing applications.

For, three-input high-base optical computing, an innovative scheme to perform graphene-assisted modulo 4 functions of three-input high-base optical computing is presented. By

exploiting multiple nondegenerate FWM processes in a single-layer graphene-coated fiber device and adopting (D)QPSK signals, we experimentally demonstrate 10-Gbaud modulo 4 operations of three-input quaternary hybrid addition and subtraction of A+ B − C, A + C − B, and B + C − A, respectively. Additionally, in order to verify the enhancement of graphene-coated fiber device, we measure the output spectrum without graphene for reference under the same experimental conditions. Moreover, we repeat the experiment by adding extra 2 and 5 m single-mode fibers in the set-up and get almost the same experimental results. The nondegenerate FWM processes in graphene-assisted nonlinear optical devices (e.g., graphene coated fiber device) are enhanced by comparing the conversion efficiency between the two cases with and without graphene.

For, GSMR-enhanced all-optical up and down wavelength conversion, using the graphene-assisted nonlinear optical device, we experimentally demonstrate up and down wavelength conversion of a 10-Gbaud quadrature phase-shift keying (QPSK) signal by exploiting degenerate four-wave mixing (FWM) progress in the fabricated GSMR. To enhance the nonlinear interactions in silicon waveguide devices, resonator structures such as microring resonators can be introduced. Graphene can be also utilized to enhance the nonlinear interactions in silicon waveguide devices. So, in order to further enhance the nonlinearity of silicon microring resonator, the GSMR is fabricated. It is expected that the GSMR might find more interesting on-chip optical signal-processing applications.

Actually, there are different platforms for nonlinear optical signal processing, e.g., silica in fiber, silicon, and graphene. **Table 1** summarizes a brief comparison among silica in fiber, silicon, and graphene. The Kerr coefficients of silica in fiber, silicon, and graphene are $\sim 10^{-20}$, $\sim 10^{-18}$, and $\sim 10^{-11}$ m²/W, respectively. Nonlinear optical signal processing based on silica in fiber has lower power loss. Although silica in fiber is compatible with optical fiber transmission systems, its third-order nonlinearity is lower and the desired fiber is longer (i.e., larger footprint). Silicon has higher $\chi^{(3)}$ nonlinearity and the compactness of silicon photonic device is suitable for chip-scale optical signal processing functions. However, silicon photonic device is not compatible with optical fiber transmission systems. In contrast, graphene has even larger $\chi^{(3)}$ nonlinearity and the fabricated graphene-assisted nonlinear optical fiber device with the graphene placed within the connector of two fibers is fully compatible with existing optical fiber transmission systems. The $\chi^{(3)}$ nonlinearity of graphene is several orders of magnitude larger than silica in fiber and silicon, which is due to the unique linear band structure of π-electrons [12, 36, 37]. The graphene-assisted nonlinear optical fiber device is compact. The combined effective nonlinearity of graphene-assisted nonlinear optical fiber device is increased and the graphene enhances the FWM process. However, the measured conversion efficiency of graphene-assisted nonlinear optical fiber device in the experiment is ~33 dB, which is lower than highly nonlinear fiber. It is noted that practically fabricated graphene is not perfect and any imperfections during the fabrication of graphene can break the band structure and degrades the dispersionless and $\chi^{(3)}$ nonlinearity properties. Additionally, the FWM conversion efficiency is also dependent on the number of graphene layers. Previous work demonstrated that the nonlinear response of graphene was sensitive to the number of graphene layers [12]. It is expected that for a few graphene layers the nonlinearity increases in proportion to the number of layers, suggesting the tremendous potential of graphene as a

Platforms	Kerr coefficient	Loss	Compactness	Compatibility*
Silica in fiber [38]	$\sim 10^{-20}$ m^2/W	Low	Large footprint	Fully compatible
Silicon [39]	$\sim 10^{-18}$ m^2/W	High	Compact	Incompatible
Graphene-coated fiber [13]	$\sim 10^{-11}$ m^2/W	Low	Compact	Fully compatible

*Compatibility of silica in fiber, silicon photonic device, and graphene-assisted nonlinear optical fiber devices with existing optical fiber transmission systems.

Table 1. Comparison among silica, silicon, and graphene.

platform for efficient nonlinear optical signal processing. In this scenario, it is possible to further enhance the FWM response by appropriately increasing the number of graphene layers employed in the experiment.

As mentioned above, a silicon photonic device is not compatible with optical fiber transmission systems. However, silicon has higher $\chi^{(3)}$ nonlinearity and the compactness of the silicon photonic device is suitable for chip-scale optical signal processing functions. Recently, silicon waveguides used as wavelength converters have shown some superior performance compared with SOA, HNLFs, and PPLN. The advantages of silicon waveguide-based wavelength converters are as follows: (1) in silicon waveguides, high-contrast index leads to tight light confinement and the nonlinear effects are greatly enhanced; (2) silicon waveguides also feature broad bandwidth, high speed, low cost, low power consumption, and complementary metal-oxide-semiconductor (CMOS) compatibility. However, the conversion efficiency of FWM in the silicon waveguides is fundamentally hampered by the large nonlinear losses of silicon, which is caused by two-photon absorption (TPA) and free carrier absorption (FCA) in silicon [40]. Therefore, the saturation of the conversion efficiency is consequence of the nonlinear absorption increment when the intensity of the input light reaches a certain level at the near-infrared region. The incorporation of reverse biased p-i-n junctions in the silicon waveguides can remove the free carrier and fasten the lifetime of the free carrier. In such a way, the conversion efficiency of FWM is increased [41]. However, the external electric modulation gives rise to the power consumption which is not available for large-scale photonic integration. Graphene has a third-order nonlinear susceptibility which is several orders of magnitude larger than that of silicon. When the monolayer graphene is transferred on the silicon waveguides, the nonlinear optical performances of the device are enhanced owing to the evanescently coupling between the silicon waveguide and graphene over a distance of hundreds of micrometers [14, 15]. Therefore, combination of the giant nonlinearity of graphene and the strong electromagnetic field confinement of silicon waveguides may be an interesting way for all optical signal processing.

Acknowledgements

Author details

Jian Wang* and Xiao Hu

*Address all correspondence to: jwang@hust.edu.cn

Wuhan National Laboratory for Optoelectronics, School of Optical and Electronic Information, Huazhong University of Science and Technology, Wuhan, Hubei, China

References

[1] K. S. Novoselov, A. K. Geim, S. V. Morozov, D. Jiang, Y. Zhang, S. A. Dubonos, and A. A. Firsov, "Electric field effect in atomically thin carbon films." Science 306, 666–669 (2004).

[2] K. Kim, J. Y. Choi, T. Kim, S. H. Cho, and H. J. Chung, "A role for graphene in silicon-based semiconductor devices." Nature 479, 338–344 (2011).

[3] F. Xia, T. Mueller, Y. M. Lin, A. Valdes-Garcia, and P. Avouris, "Ultrafast graphene photodetector." Nat. Nanotechnol. 4, 839–843 (2009).

[4] Q. Bao, H. Zhang, B. Wang, Z. Ni, C. H. Y. X. Lim, Y. Wang, and K. P. Loh, "Broadband graphene polarizer." Nat. Photonics 5, 411–415 (2011).

[5] M. Liu, X. Yin, E. Ulin-Avila, B. Geng, T. Zentgraf, L. Ju, and X. Zhang, "A graphene-based broadband optical modulator." Nature 474, 64–67 (2011).

[6] A. Grigorenko, M. Polini, and K. Novoselov, "Graphene plasmonics." Nat. Photonics 6, 749–758 (2012).

[7] Q. Bao, H. Zhang, Y. Wang, Z. Ni, Y. Yan, Z. X. Shen, K.P. Loh, and D. Y. Tang, "Atomic-layer graphene as a saturable absorber for ultrafast pulsed lasers." Adv. Fun. Mat. 19, 3077–3083 (2009).

[8] Z. Sun, T. Hasan, F. Torrisi, D. Popa, G. Privitera, F. Wang, F. Bonaccorso, D. M. Basko, and A. C. Ferrari, "Graphene mode-locked ultrafast laser." ACS Nano 4, 803–810 (2010).

[9] Q. Bao, H. Zhang, Z. Ni, Y. Wang, L. Polavarapu, Z. Shen, Q. Hua, D. Tang, and K. P. Loh, "Monolayer graphene as a saturable absorber in a mode-locked laser." Nano Res. 4, 297–307 (2011).

[10] Y. Meng, S. Zhang, X. Li, H. Li, J. Du, and Y. Hao, "Multiple-soliton dynamic patterns in a graphene mode-locked fiber laser." Opt. Express 20, 6685–6692 (2012).

[11] N. Tolstik, E. Sorokin, and I. T. Sorokina, "Graphene mode-locked Cr: ZnS laser with 41 fs pulse duration." Opt. Express 22, 5564–5571 (2014).

[12] E. Hendry, P. J. Hale, J. Moger, A. K. Savchenko, and S. A. Mikhailov, "Coherent nonlinear optical response of graphene." Phy. Rev. Lett. 105, 097401 (2010).

[13] H. Zhang, S. Virally, Q. Bao, K.P. Loh, S. Massar, N. Godbout, and P. Kockaert, "Z-scan measurement of the nonlinear refractive index of graphene." Opt. Lett. 37, 1856–1858 (2012).

[14] T. Gu, N. Petrone, J. F. McMillan, A. van der Zande, M. Yu, G. Q. Lo, D. L. Kwong, J. Hone, and C. W. Wong, "Regenerative oscillation and four-wave mixing in graphene optoelectronics." Nat. Photonics, 6, 554–559 (2012).

[15] H. Zhou, T. Gu, J. F. McMillan, N. Petrone, A. van der Zande, J. C. Hone, and S. Zhou, "Enhanced four-wave mixing in graphene-silicon slow-light photonic crystal waveguides." Appl. Phys. Lett. 105, 091111 (2014).

[16] B. Xu, A. Martinez, K. Fuse, and S. Yamashita, "Generation of four wave mixing in graphene and carbon nanotubes optically deposited onto fiber ferrules." OSA. CLEO: Science and Innovations, CMAA6, 2011.

[17] Y. Wu, B. Yao, Y. Cheng, Y. Rao, Y. Gong, X. Zhou, B. Wu, and K. S. Chiang, "Four-wave mixing in a microfiber attached onto a graphene film." IEEE Photonics Techno. Lett. 26, 249–252 (2014).

[18] Y. Wu, B. C. Yao, Q. Y. Feng, X. L. Cao, X. Y. Zhou, Y. J. Rao, and K. S. Chiang, "Generation of cascaded four-wave-mixing with graphene-coated microfiber." Pho. Res. 3, A64–A68 (2015).

[19] B. Xu, A. Martinez, and S. Yamashita, "Mechanically exfoliated graphene for four-wave-mixing-based wavelength conversion." IEEE Photonics Techno. Lett. 20, 1792–1794 (2012).

[20] P. J. Winzer, and R J. Essiambre, "Advanced modulation formats for high-capacity optical transport networks." J. Lightwave Techno. 24, 4711–4728 (2006).

[21] X. Hu, M. Zeng, A. Wang, L. Zhu, L. Fu, and J. Wang, "Graphene-assisted nonlinear optical device for four-wave mixing based tunable wavelength conversion of QPSK signal." Opt. Express 23, 26158–26167 (2015).

[22] A. Wang, X. Hu, L. Zhu, M. Zeng, L. Fu, and J. Wang, "Experimental demonstration on two-input optical high-base hybrid doubling and subtraction functions in graphene." Opt. Express 23, 31728–31735 (2015).

[23] X. Hu, A. Wang, M. Zeng, Y. Long, L. Zhu, L. Fu, and J. Wang, "Graphene-assisted multiple-input high-base optical computing." Sci. Rep. 6, 1–5 (2016).

[24] X. Hu, Y. Long, M. Ji, A. Wang, L. Zhu, Z. Ruan, Y. Wang, and J. Wang, "Graphene-silicon microring resonator enhanced all-optical up and down wavelength conversion of QPSK signal." Opt. Express, 24, 7168–7177 (2016).

[25] F. Bonaccorso, Z. Sun, T. Hasan, and A. C. Ferrari, "Graphene photonics and optoelectronics." Nat. Photonics 4, 611–622 (2010).

[26] Q. Bao, and K. P. Loh, "Graphene photonics, plasmonics, and broadband optoelectronic devices." ACS Nano 6, 3677–3694 (2012).

[27] B. Sensale-Rodriguez, R. Yan, M. M. Kelly, T. Fang, K. Tahy, W. S. Hwang, and H. G. Xing, "Broadband graphene terahertz modulators enabled by intraband transitions." Nat. Commun. 3, 1–7 (2012).

[28] X. Li, W. Cai, J. An, S. Kim, J. Nah, D. Yang, and S. K. Banerjee, "Large-area synthesis of high-quality and uniform graphene films on copper foils." Science. 324, 1312–1314 (2009).

[29] M. Kalbac, A. Reina-Cecco, H. Farhat, J. Kong, L. Kavan, and M. S. Dresselhaus, "The influence of strong electron and hole doping on the Raman intensity of chemical vapor-deposition graphene." ACS Nano 4, 6055–6063 (2010).

[30] M. Jablan, H. Buljan, and M. Soljačić, "Plasmonics in graphene at infrared frequencies." Phys. Rev. B 80, 245435 (2009).

[31] A. Pasquazi, R. Ahmad, M. Rochette, M. Lamont, B. E. Little, S. T. Chu, and D. J. Moss, "All-optical wavelength conversion in an integrated ring resonator." Opt. Express. 18, 3858–3863 (2010).

[32] F. Morichetti, A. Canciamilla, C. Ferrari, A. Samarelli, M. Sorel, and A. Melloni, "Travelling-wave resonant four-wave mixing breaks the limits of cavity-enhanced all-optical wavelength conversion." Nat. Commun. 2, 296 (2011).

[33] M. Ji, H. Cai, L. Deng, Y. Huang, Q. Huang, J. Xia, and Y. Wang, "Enhanced parametric frequency conversion in a compact silicon-graphene microring resonator." Opt. Express. 23, 18679–18685 (2015).

[34] X. Wang, J. A. Martinez, M. S. Nawrocka, and R. R. Panepucci, "Compact thermally tunable silicon wavelength switch: modeling and characterization." IEEE Photonics Technol. Lett. 20, 936–938 (2008).

[35] F. Gan, T. Barwicz, M. A. Popovic, M. S. Dahlem, C. W. Holzwarth, P. T. Rakich, and F. X. Kartner, "Maximizing the thermos-optic tuning range of silicon photonic structures." Photon. in Switching 19, 67–68 (2007).

[36] A. K. Geim, and K. S. Novoselov, "The rise of graphene." Nat. Mat. 6, 183–191 (2007).

[37] K. S. Novoselov, A. K. Geim, S. V. Morozov, D. Jiang, M. I. Katsnelson, I. V. Grigorieva, S. V. Dubonos, and A. A. Firsov, "Two-dimensional gas of massless Dirac fermions in graphene." Nature 438, 197–200 (2005).

[38] L. Prigent and J.-P. Hamaide, "Measurement of fiber nonlinear Kerr coefficient by four-wave mixing." Photonics Techno. Lett. IEEE 5, 1092–1095 (1993).

[39] M. Dinu, F. Quochi, and H. Garcia, "Third-order nonlinearities in silicon at telecom wavelengths." Appl. Phys. Lett. 82, 2954–2956, 2003.

[40] T. Uesugi, B. S. Song, T. Asano, and S. Noda, "Investigation of optical nonlinearities in an ultra-high-Q Si nanocavity in a two-dimensional photonic crystal slab," Opt. Express 14, 377–386 (2006).

[41] A. Gajda, L. Zimmermann, M. Jazayerifar, G. Winzer, H. Tian, R. Elschner, T. Richter, C. Schubert, B. Tillack, and K. Petermann, "Highly efficient CW parametric conversion at 1550 nm in SOI waveguides by reverse biased p-i-n junction," Opt. Express 20, 13100–13107 (2012).